Correlations between Synthesis and Performance of Fe-based PGM-free Catalysts in Acidic and Alkaline Media: Evolution of Surface Chemistry and Morphology

Kateryna Artyushkova[1a], Santiago Rojas-Carbonell[1a], Carlo Santoro[a], Elizabeth Weiler[a],*

Alexey Serov[b], Roxanne Awais[a], Rohan Rajeev Gokhale[a], Plamen Atanassov[a, c]

[1] The two authors have equally contributed to the manuscript

[a]Department of Chemical and Biological Engineering, Center for Micro-Engineered Materials (CMEM), The University of New Mexico, Albuquerque, NM 87131, USA.

[b] Pajarito Powder, LLC, 3600 Osuna Rd NE, Suite 309, Albuquerque, NM 87109, USA.

[c]Department of Chemical and Biomolecular Engineering, Fuel Cells Research Center, University of California, Irvine, CA 92697, USA.

KEYWORDS

Oxygen reduction reaction, PGM-free catalyst, acid electrolyte, alkaline electrolyte, surface chemistry and morphology

ABSTRACT

The effects of the synthesis steps of a platinum group metal-free (PGM-free) catalyst on the surface chemistry, morphology and electrochemical activity in acidic and alkaline media towards the oxygen reduction reaction (ORR) were studied. Each step exhibits a positive impact on catalyst activity. In acid media, etching of the silica template is the major contributor to the enhancement of the half wave potential, as the ORR active sites formed during the first pyrolysis become more accessible. Further processing steps result even in higher accessibility and utilization of the 4e- transfer sites. In alkaline media, the second pyrolysis is a critical step that favors the complete reduction of oxygen to water, as the peroxide production is significantly diminished. The large heterogeneity in the porosity at each synthesis step indicates that this parameter needs to be further studied to attain better control of the morphology of the PGM-free catalyst, as it is an important factor that contributes to the active site utilization. The acid etching and second pyrolysis increase the meso- and macroporosity. Understanding the effects of each of the synthesis steps on the chemical composition, morphology and ORR activity of the PGM-free catalyst provides the necessary feedback for the design of synthetic schemes that increase the catalysts' performance.

INTRODUCTION

In proton exchange membrane (PEM) and anion exchange membrane (AEM) fuel cells, one of the critical factors affecting the overall efficiency and performance is the kinetics of oxygen reduction reaction (ORR). To address this limitation, a plethora of efforts are being put into optimizing the chemical and structural properties of catalysts. Platinum is the state-of-the-art cathode catalyst in PEMFCs due to its high catalytic activity and stability in a highly acidic operating pH. In parallel, in AEM fuel cells, one of the most active and stable catalysts utilized is

palladium or palladium based alloys.[1] Due to limited sources of Pt and Pd, as well as their high cost, different strategies have been adopted to either decrease the PGM amounts or eliminate the use of Pt. Significant progress has been made in replacing PGM with PGM-free materials based on transitional metal compounds, such as nitrides/carbides[2–4] or chalcogenides.[5–7]

Nitrogen-containing M-N-C catalysts are usually synthesized from a mixture of a transition metal salt and organic precursors rich in nitrogen that is subjected to high-temperature treatment between 600°C and 1100°C in an oxygen-free controlled atmosphere. The resulting materials exhibit a large degree of porosity, surface area, and graphitization. This graphitic carbon network possesses nitrogen and transition metal defects. The chemistry of these transition metal-nitrogen-carbon composites has been studied extensively by a combination of spectroscopic techniques such as Mossbauer,[8] X-ray Photoelectron Spectroscopy (XPS),[9–15] X-ray Absorption Spectroscopy (XAS)[16,17] and theoretical modeling such as Density Functional theory.[18–28] XPS has been proven to be one of the analytical techniques that provide a surface concentration of M-N-C catalysts from top 5-11 nm of the surface, which is directly related to the electrochemical performance of these catalysts. Multiple structure-to-property studies based on the correlation between XPS surface composition and performance have advanced the development of M-N-C catalysts for ORR.[2,9–12,14,29–34]

The backbone of the material is a carbon network which is rich in surface oxides at the edges.[10] In addition to carbon-oxygen defects, there is a multitude of nitrogen defects, located in both edges and in-plane graphene matrixes. [9,18,35] The edges of the carbonaceous material may be terminated by imine and amine groups, pyridinic nitrogen, hydrogenated nitrogen (pyrrolic and hydrogenated pyridine), quaternary, and N-O groups[17,36,37] within the plane of the carbonaceous material, graphitic nitrogen, and nitrogen coordinated with iron in a variety of configurations FeN_x-C, where

x=1-4 are also present.[37] The preferential chemical state of iron is iron coordinated by nitrogen. However, some residual amounts of iron-rich phase, such as iron oxide, iron carbide, and iron metal nanoparticles may be present.

Due to the plurality of chemical moieties present in the M-N-C materials, the oxygen reduction reaction may occur via several parallel pathways, *i.e.*, (i) the desirable $4e^-$ a direct reduction of oxygen to water, (ii) the undesirable for fuel cell applications $2e^-$ partial reduction of oxygen to hydrogen peroxide and (iii) the subsequent $2x2e^-$ reduction of peroxide to water.

There is an agreement in the community that atomically dispersed iron coordinated to nitrogen catalyzes a full $4e^-$ reduction to water. Multiple experimental confirmations have been published recently for the family of materials presented herein. [9,10,12,15,35] In parallel, the hydrogenated and protonated nitrogen catalyzes the production of hydrogen peroxide intermediate, and higher concentrations of these nitrogen species contribute to lower catalytic activity towards $4e^-$ mechanism. [9–11,15] At the same time, pyridinic nitrogen was shown to catalyze the reduction of peroxide to water, contributing to better overall efficiency by converting the intermediate peroxide formed into the water. [9,10]

As a result of these thorough structure-to-property investigations [9,31,35], there is an understanding of which types of structures would be desired or undesired in the electrocatalyst for increased efficiency of ORR, i.e., it has to have larger amounts of atomically dispersed FeN_x-C centers, pyridinic N, as well as small amounts of hydrogenated and protonated edge sites.

Understanding the chemistry of the active site is often combined with a broadly accepted hypothesis that the microporous portion of catalysts plays a critical role in forming the active site.[33] Transport behavior of gases within the support, accessibility of active sites, and electronic conductivity of the support are affected by the morphology of the support, which has not been

studied in detail.[38] Surface morphology is one of the most crucial factors affecting the functional performance of heterogeneous multiscale M-N-C materials.

Hence, it is critically important to build an understanding of interdependencies between the catalyst synthesis steps and the resulting chemistry and morphology of the same. It will be a salient input for designing synthetic routes to simultaneously and selectively control the catalyst's chemistry and morphology

A typical synthesis of the M-N-C materials involves multiple steps, each of them affecting chemistry and morphology of the resulting electrocatalyst. The sacrificial support method (SSM), starts by pyrolyzing a well-dispersed suspension of a silica template, a metal salt, and nitrogen-rich organic precursors. After pyrolyzing this mixture, the silica template is removed through etching. The removal of silica increases the surface area of the catalysts significantly. The best performing catalysts have been obtained by the five-step synthesis: i) the first pyrolysis; ii) first ball milling; iii) etching away the silica and excess of Fe-rich phase; iv) second pyrolysis and v) second ball milling. [9,31,35,39]

In this manuscript, the effect of each synthesis step on the electrocatalytic ORR activity in acidic and alkaline media is investigated and correlated to the surface chemistry and morphology changes introduced during the synthesis. The surface chemistry was studied by XPS, while morphology was examined using scanning electron microscopy (SEM). The ORR activity was investigated via the rotating ring disk electrode technique (RRDE), and the electrochemical parameters such as potential at the kinetic current of 100 μA cm^{-2}, half-wave potential, limiting current and peroxide generation were determined. The relationships between the surface chemistry and morphology to the electrochemical parameters at each one of the five synthesis steps are presented and discussed

in detail. These results provide insights for targeted improvements in the synthesis of active catalysts in the future.

2. EXPERIMENTAL METHODS

2.1 CATALYST SYNTHESIS

The catalyst was prepared using Sacrificial Support Method (SSM) technique adopting silica as a hard-templating agent. The procedure starts by first making a homogeneous mixture of the precursors, which then undergoes the five synthesis steps. For the homogeneous mixture, the organic precursor, the metal salt and the silica were combined. 55.6%wt of Nicarbazin (Sigma-Aldrich, 98%) as a nitrogen-rich organic precursor, 5.6%wt. of iron nitrate nonahydrate (Sigma-Aldrich, 99.95%) as a metal salt, 11.0%wt. of Stöber spheres (in house made), 13.9%wt. of LM-150 fumed silica (Cabot); 13.9%wt. of OX-50 hydrophilic fumed silica (Aerosil) as templates were mixed in a glass beaker using DI water while stirring the solution overnight at a temperature of 45°C. The next day, the solution was transferred into an oven set at 85°C for 16 h to remove the remaining water content. The mixture was ground using a planetary ball miller with agate jar and balls for 30 minutes at 5.8 Hz, till fine powder was obtained.

The first synthesis step consists of the high-temperature pyrolysis of the homogenized precursor mix powder. The powder was placed into a ceramic crucible and inserted into a quartz tube. The atmosphere within the tube was composed of 7% of H_2 balanced in a flow of 100 cm^3 min^{-1} of ultra-high purity N_2 (Airgas). The role of the H_2 during the first pyrolysis is to ensure the reductive atmosphere that prevents the formation of the undesired iron oxides. The reduced iron atoms originating from the thermal decomposition of the iron nitrate will then participate in the formation of the iron-nitrogen ORR active sites.

Once the temperature of the furnace reached 575°C, the tube was inserted into the furnace, and the temperature was further increased to 900°C with a ramp of 75°C min^{-1}. After that, the temperature was increased further to 975°C with a ramp of 10°C min^{-1}. The obtained material was left for 45 minutes at 975°C and then taken out of the oven to naturally cool down to room temperature under the same reductive conditions (7% of H_2).

In the second step, the cooled material was ground using a planetary ball mill with agate milling media at a frequency of 5.8 Hz for 30 minutes.

The third stage of the process was the etching the silica template by leaving the material to react for three days in a mixture of HF (48 wt. % in H_2O, ≥99.99% trace metals basis) and HNO_3 (70%, ≥99.999% trace metals basis) in ratio 2:1. The powder was then washed with DI water until a neutral pH of the supernatant was achieved and then dried for 16 hours at 85°C to remove the excess in water.

The fourth stage of the process involved the second pyrolysis, in which the powder underwent the second heat treatment. The conditions of the thermal treatment were the same as the first one with the only difference being the utilization of 7% ammonia (Matheson, Semicon 5N, 99.999%) instead than H_2. After 45 minutes hold at a constant temperature, the sample was cooled down to ambient temperature under the same conditions (7% ammonia).

The fifth and last phase included ball milling of the powder using agate glassware at 5.8 Hz for 30 minutes.

Three catalyst batches were fabricated in parallel, each of the final batches weighing about 4.5g. During each synthesis phase, a small amount of sample was conserved to analyze the surface chemistry, surface morphology, and electrochemical activity. The catalysts tested in this work are presented in Table 1.

Table 1. Catalysts samples for each batch and each phase during the preparation.

sample number	batch	1st pyrolysis	1st ball milling	Acid etching	2nd pyrolysis	2nd ball milling	sample abbreviation
1	1	x					P-1
2	2	x					P-2
3	3	x					P-3
4	1	x	x				PB-1
5	2	x	x				PB-2
6	3	x	x				PB-3
7	1	x	x	x			PBE-1
8	2	x	x	x			PBE-2
9	3	x	x	x			PBE-3
10	1	x	x	x	x		PBE2P-1
11	2	x	x	x	x		PBE2P-2
12	3	x	x	x	x		PBE2P-3
13	1	x	x	x	x	x	PBE2PB-1
14	2	x	x	x	x	x	PBE2PB-2
15	3	x	x	x	x	x	1PBE2PB-3

2.2. SURFACE CHEMISTRY

High-resolution X-ray Photoelectron Spectroscopy (XPS) was performed using Kratos DLD spectrometer with a monochromatic Al Kα source operating at 225mW. Three areas per sample were analyzed. The results presented are the averages from there areas together with standard deviations calculated. Samples A1-A3 were analyzed with the assistance of charge neutralizer (CN), while the rest of the samples did not require the use of CN. CasaXPS was used to process the data. A 70% Gaussian/30% Lorentzian line shape was utilized in the curve-fit of spectra. The

linear background was used for quantifying atomic composition except for Fe 2p spectra, for which Shirley background was used. High-resolution spectra were fitted according to the procedure established previously. [10,15,31]

2.3 SURFACE MORPHOLOGY

SEM imaging was performed using Hitachi S-5200 UHR FE-SEM at 2 kV in SE mode at 50k magnification. Six images were acquired from six different areas on the samples to capture an overall representation of morphology. To ensure that the intensity variation is caused by the sample morphology and not by the different instrumental conditions, all the images were recorded at the same experimental settings (i.e., voltage, magnification, brightness and contrast, current and gain). Digital image processing (DIP) was done using an in-house developed GUI in Matlab using the Image Processing Toolbox as shown previously. [40] This technique has been verified via nitrogen adsorption measurements on M-N-C catalysts. [41]

High pass filtering of images was done to remove the low-frequency component resulting in images capturing features between 8 and 60 nm, while low pass filtering was done to remove high-frequency component resulting in images capturing features between 100 and 400 nm.[42] Skewness parameter was calculated from overall filtered images to describe relative porosity at two different scales that may be related to different properties of catalysts. Skewness is calculated from the image histogram, and it defines the extent to which a distribution differs from a normal distribution. Larger porosity expressed by larger pore size and larger density of pores will result in smaller skewness of the image. [41–44]

The following areal parameters were calculated from thresholded original images: 1) Solid size, which is measured as the average number of pixels (converted to nm) where the catalyst solid

phase is present in x and y-direction; 2) Pore size, measured as the number of consecutive pixels (converted to nm) where no material is present in x and y-direction (only solid and pore size in x-direction was included in results, as there is no anisotropy in the morphology) and 3) Areal porosity, i.e., the ratio of empty pixels (without material) to total area.

2.4 ELECTROCHEMICAL MEASUREMENTS

The electrochemical performances were measured using a rotating ring disk electrode (RRDE) technique. The catalysts during each synthesis phase of the three different batches were tested in acidic and alkaline media electrolyte. A total of 5 mg of each catalyst was inserted into a plastic vial with 850 µL of a mixture with a 4:1 ratio of DI water and IPA (Sigma, ≥99.7%) and 150 µL of 0.5%wt of Nafion (FuelCell Store). The resulted catalyst concentration was 5 µg μL^{-1}. The ink was horn sonicated three times for 5 minutes each time. A pipette was used to take the ink from the plastic vial and drop cast it to the disk electrode. The RRDE had a disk with an area of 0.2475 cm^2 and a ring with an area of 0.1866cm^2. The ink was left to dry at ambient temperature and pressure. The previously optimized catalyst loading was 0.175 mg cm^{-2},[10] and it has been established that this loading is enough to cover the RRDE disk without introducing additional diffusion barrier for the detection of the peroxide in the ring. To obtain this loading, 8.7 µL of the catalyst ink was deposited on the disk electrode. RRDE was run in two electrolytes: 0.5 M H_2SO_4 (in house prepared using Sigma, 99.999%) for acidic media and 0.1 M KOH (in house prepared using BioXtra, ≥85% KOH basis) for alkaline media. The electrolyte was initially flushed vigorously with pure oxygen (for at least 20 minutes and then continuously bubbled through the experiment. Linear sweep voltammetry (LSV) was performed using the disk as a working electrode, a graphite rod as a counter electrode and an RHE reference electrode connected to the

corresponding channel. RRDE was rotating at a constant speed of 1600 rpm. The potential window investigated was between 1.1 V and 0 V vs. RHE in both media. The ring potential was held at a 1.1 V vs. RHE to detect the peroxide produced at the disk. The catalysts were preconditioned by performing cyclic voltammetry at a rate of 50mV s^{-1}. After this preconditioning cycle, a steady LSV was observed, and new LSVs were run as cathodic sweeps at a scan rate of 5 mV s^{-1}. The capacitance of the catalyst layer was corrected by analyzing the current at 1V vs RHE, where no activity of the PGM-free catalyst was observed. The disk current density (j_{disk}) and ring current density (j_{ring}) were used to estimate the hydrogen peroxide yield ($\%H_2O_2$) and the number of electrons transferred (n) according to equation 1 (eq. 1) and 2 (eq. 2) respectively. N represents the ring collection efficiency of 37%.

$$n = \left| \frac{4 j_{disk}}{j_{disk} + \frac{j_{ring}}{N}} \right| \qquad \text{(eq.1)}$$

$$\%H_2O_2 = \frac{(4-n)}{2} * 100 \qquad \text{(eq. 2)}$$

2.5 SURFACE CHEMISTRY AND MORPHOLOGY RELATIONSHIP WITH ELECTROCHEMISTRY

The relationship between surface chemistry, morphology and performance were studied with the assistance of principal component analysis (PCA). PCA is a multivariate statistical tool, commonly used to reduce the dimensionality of large data sets and to express the data in a way that highlights similarities and differences between samples and variables. PCA provides the ability to identify the major structural and morphological factors influencing electrochemical performance. In PCA,

two input data tables were created – one combining XPS atomic concentrations and chemical speciation (Figure 1S d) with electrochemical parameters (limiting current densities and half-wave potential in acid and alkaline) and the other combining morphological parameters with the same electrochemical parameters. PCA transforms the experimental data matrix into a smaller number of principal components, each having a score and loading associated with it. The loadings are a linear combination of the original variables. The 2 principal components corresponding to the largest 2 eigenvalues, captures the most variance in the data, while the remaining components, each describing a low variance, represent the noise in the data set. The results of PCA are usually displayed as biplots reflecting the significance of each sample in a principal component (scores) and reflecting the significance of each variable in a principal component (loadings).

3. RESULTS AND DISCUSSION

3.1 CATALYST SURFACE CHEMISTRY

Elemental composition and speciation of catalysts at each step of synthesis were presented and discussed in detail in our previous publication.[39,43] Table S1 shows all elements detected by the low-resolution XPS survey spectra. In the precursor mixture, 13% of Si from a template is present. A large amount of oxygen is also detected. The first pyrolysis causes an increase in carbon concentration at the expense of a decrease of surface oxides. Ball milling serves as another cleaning step in which the amount of both oxygen and Si decreases. Etching removes template very efficiently as confirmed by the absence of Si 2p peak. A small amount of F from HF cleaning is detected. The 2nd pyrolysis causes a decrease in oxygen with almost 90% of the carbon present. No F and Si are detected in the pyrolyzed product at the end of all synthetic steps. Figure S1 shows the curve-fitted high-resolution spectra along with quantitative results extracted from the spectra,

while Figure 1 shows the main observations in the evolution of chemistry during each step of the synthesis. After the first pyrolysis, a high amount of oxygen - up to 35 at % - was detected at the surface. The first ball milling step introduces a small change in composition by decreasing the amount of oxygen at the surface slightly. However, the major change in the removal of surface oxides occurs during the etching process. After etching, only 10 at% of oxygen is detected, and carbon increases to above 80 at%, which is expected due to the removal of the silicon oxide. This is also the stage after which a larger amount of nitrogen is exposed to the surface due to the removal of extra surface oxides. Very small changes are occurring in elemental composition during the second pyrolysis and second ball milling. This is also true for changes within the chemistry of the carbon. Surface oxides C_xO_y are removed during the first ball milling and etching with stable carbon chemistry achieved after the etching step. This confirms that surface oxides are mainly present at the surface and milling homogenizes the chemistry and redistributes its composition within the total volume of material.

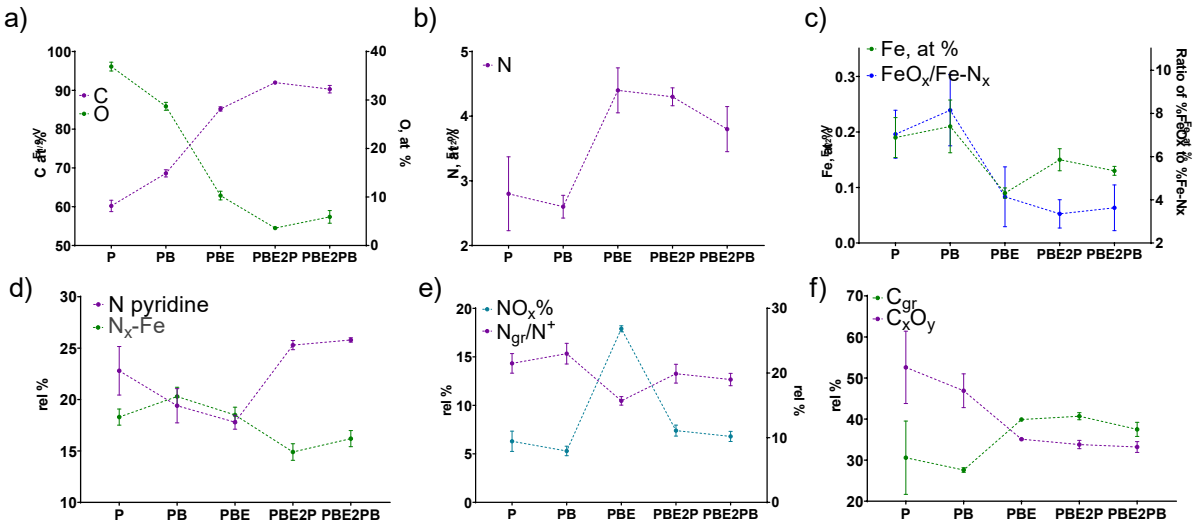

Figure 1. Evolution of surface chemistry through the five synthesis steps atomic % for a) C and O; b) N, c) Fe (left y-axis) and ratio between relative % of Fe oxides and Fe-N_x species (right y-axis).

Relative % for species obtained from fitted N 1s and c 1s spectra d) pyridinic N and N_x-Fe/NH_2, e) N^+/N_{gr} (left y-axis) and NO_x (right y-axis) and f) CxOy and Cgr. Adapted from[39] under a Creative Commons license ((CC BY 4.0)), copyright 2018 Elsevier.

The changes in nitrogen chemistry are observed throughout all the synthesis steps. The etching causes the formation of high amounts of nitrogen oxides at the surface with other types of nitrogen being at their lowest surface concentrations at this stage of synthesis. The second pyrolysis serves as a major step in "cleaning" and "activating" the catalyst surface. During this step, nitrogen oxide species are being removed, and a large amount of edge pyridinic nitrogen is being formed. Iron also undergoes major change – after the first pyrolysis and ball-milling majority of iron is present as Fe oxides FeO_x species as is shown in FeO_x/Fe-N_x ratio in Figure 1 c), right axis. No metallic Fe is observed. A dramatic decrease in the relative amount of iron oxides occurs during etching, with the much smaller relative amount of oxides with respect to Fe-N_x species.

Another role of the second pyrolysis is removing volatile SiF_x, formed during the etching step, from the porous body of catalysts as confirmed by the absence of both F and Si at the surface by XPS (Table S1). This increases the utilization of active sites. The second ball-milling step slightly increases the pyridinic and iron coordinated nitrogen, due to the increased surface exposure caused by the breakage of the larger particles.

An important observation from the evolution of chemical composition is a decrease in heterogeneity in the surface composition with each consecutive step of the synthesis. Homogenization of the surface chemistry is critical for obtaining consistent ORR activity among all the batches synthesized.

3.2 CATALYST SURFACE MORPHOLOGY

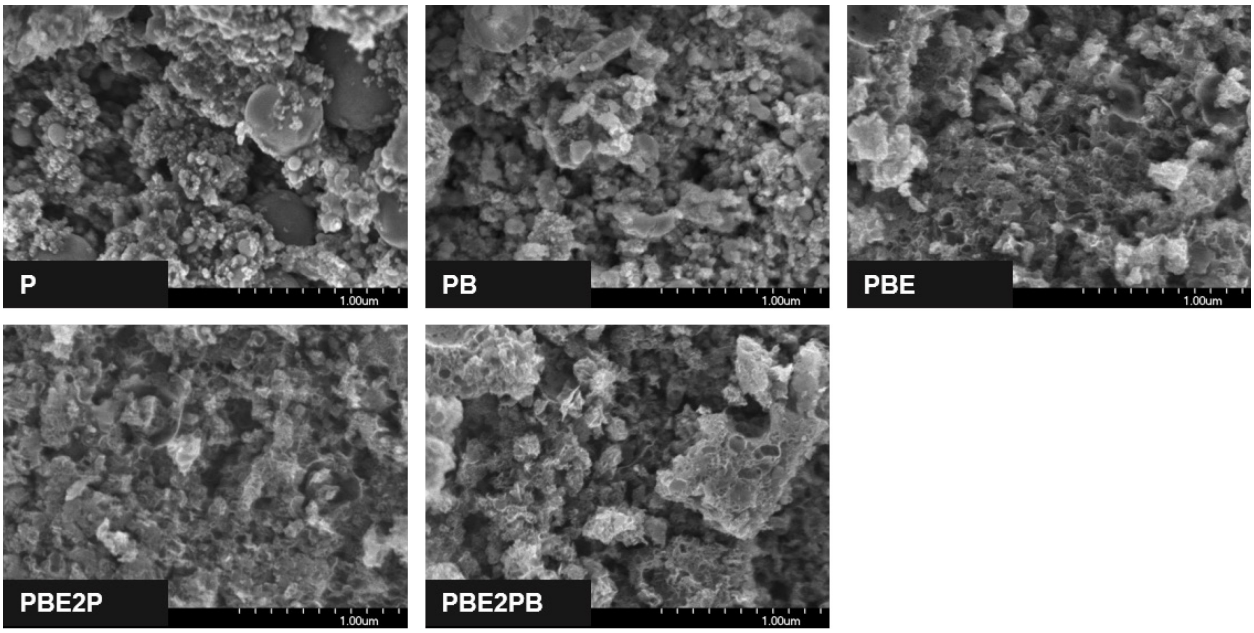

Figure 2. Evolution of surface morphology with each synthesis step. Sample SEM image out of 6 acquired is shown for each step. The magnification was 50k and the electron beam set to 2.0kV. Each segment of the scale bar in the SEM images is equivalent to 1 micron.

The interplay between chemistry and morphology of electrocatalysts and their role in oxygen reduction reaction cannot be overlooked. Figure 2 shows single SEM images obtained from the materials at each step of the synthesis. Visual inspection of individual images does not provide insight into morphological changes, as a single image may not be representative of the morphology of the whole sample. The relevant scale which promotes the formation of an effective double-layer or the transfer of ions into the pore structure are the pores within the range of 5-100 nm.[42] SEM is suitable to access these lateral dimensions and to provide sets of images representative of the morphology for statistically valid structure-to-property correlations.

For this abovementioned reason, six SEM images were obtained from six random areas of the samples, and the digital image processing (DIP) was applied to extract the material's morphological metrics, following the procedure described before.[41,43–46] The goal of DIP is to

convert 2-D images into 1-D image descriptors that can be utilized for quantitative morphology representation and description.[14,47,48] Porosity is an essential characteristic that influences the mass and transport behavior of the catalysts.[49] In our previous reports, we have shown that quantitative descriptors of morphology extracted by DIP are in strong correlation with nitrogen adsorption measurement, so they can reliably be used as macroscopic parameters.[51, 54] Skewness (R_{sk}) describes asymmetry of the roughness and points to the domination of valleys (pores) or peaks in the micrograph. Penetration of gases and ions into the pores is closely related to pore size and pore shape distributions.[50] Morphological data from overall SEM surface measurements contain information on a wide range of scales, starting from the resolution limit of the instrument used, up to the larger features capped by the field of view. Different phenomena and processes related to the material performance correspond to different diffusion regimes at different length scales, i.e. the interplay between configurational and Knudsen diffusion in mesopores (tens of nanometers) and regular diffusion in macropores (over 50 nm in diameter). Use of low-high-filtering for separating different scales of roughness is a conventional routine established for AFM images. Prior work has successfully extended this methodology to SEM images, in which high-pass and low-pass filters were employed to separate images into roughness and waviness image components, respectively.[22,23,34,51] This approach allowed splitting morphological information into two different scales.

Figure 3 shows the evolution of morphological metrics at each stage of synthesis. Skewness extracted from original images captures overall porosity. Figure S4a) shows histogram extracted from one of the multiple original images acquired for sample after the 1st pyrolysis and after the 2nd pyrolysis steps. The sample after the 1st pyrolysis contains larger portion of low grey values coming from pores than the sample after the 2nd pyrolysis. Therefore sample P will have a smaller

magnitude of skewness than sample PBE2P. Overall porosity (Figure 3a) of the materials obtained at each step is quite heterogeneous, as captured by large standard deviation, and it is very similar for materials obtained after each step of the synthesis.

The skewness calculated from the high-frequency and low-frequency component images shed more details into the changes in porosity at smaller (8-60 nm) and larger (100-400 nm) scales (Figure 3b). Figure S4 b) and c) show the histograms extracted from filtered images. The histograms of both P and PBE2P samples contributing to meso-skewness are very similar. The histograms of waviness component images contributing to macro skewness show that sample after the 1st pyrolysis has a wider distribution with larger proportion of pores (dark grey values) and peaks (bright gray values) than sample after the 2nd pyrolysis.

The trend in changes in meso- and macropores is very similar at each step. The first ball milling increases the number of pores (smaller magnitude of skewness is indicative of more pores) while etching opens the pores. The second pyrolysis causes decreases in relative amount of both mesopores and macropores homogenizing the material morphology. The last ball milling step causes a slight expansion of both meso- and macropores.

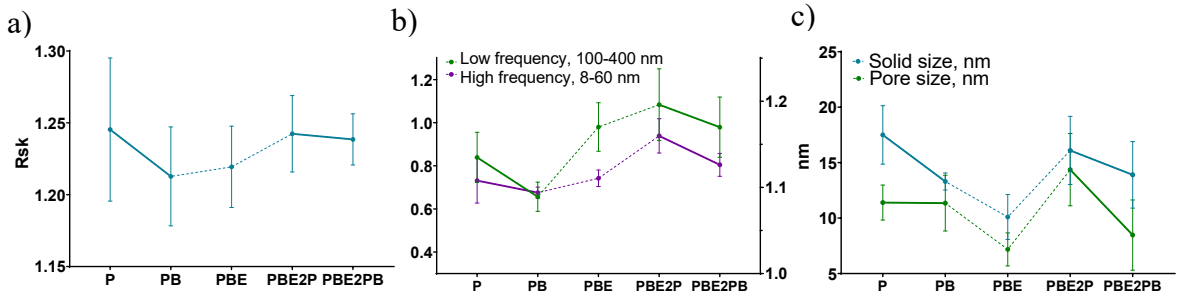

Figure 3. Evolution of surface morphological parameters extracted from SEM images for each step of the synthesis: a) overall skewness and b) filtered skewness, c) pore and solid size.

The change in the morphology was also evaluated by calculating average solid size and pore size from SEM images (Figure 3c). Ball milling and etching causes break down of larger solid clusters into smaller ones almost twice. The pores between clusters also decrease. Interestingly, the 2nd pyrolysis causes agglomeration of solid clusters and growth of pores between them almost to the initial value. The last ball milling causes break down in the solid clusters and an even larger decrease in pore size.

3.3 ELECTROCATALYTIC ACTIVITY IN ACIDIC AND ALKALINE MEDIA

To evaluate the effect each step of the synthesis has on the electrocatalytic activity, the linear sweep voltammograms for the three samples of each of the five synthesis steps were collected and reported in Figure S3. The average and standard deviation of the three LSVs was calculated. In the following figures, the disk and ring LSVs were stacked on top of each other to facilitate the comparison of the catalyst ORR activity with the peroxide formed, which is detected on the ring. From these two results, the overall electron transfer and the peroxide yield are estimated as described in the Experimental section.

3.3.1 ACIDIC MEDIA

The average LSVs for ORR activity in acid media of the PGM-free catalysts at each step of synthesis are presented in Figure 4, where j_R is in panel (a); overall e^- transferred in panel (b); j_D in panel (c) and peroxide yield in panel (d). From Figure 4c, it is clear that the successive synthesis steps make the PGM-free catalyst more active towards the ORR, particularly evidenced by the continuous increase in the half-wave potential. The ORR activity of the catalyst after the first pyrolysis and the first ball milling is very similar. The step that leads to the most significant

increase in $E_{1/2}$ is etching. The acid etching of the silica sacrificial support leads to the generation of pores on the catalysts, as well as the breakage of the larger solid clusters into smaller ones (Figure 3c). The removal of the non-conducting silica used for pore generation also leads to an increase in the electric conductivity of the PGM-free catalysts. This contributes to a larger density of active sites being accessible by the reactants, which is confirmed by the increased limiting current densities observed after the acid etching.[52]

The acid etching also caused an increase in peroxide production, as seen in Figure 4a. The oxidative etching creates a plethora of defects on the surface of the materials such as nitrogen oxides and protonated nitrogen species. The protonated nitrogen moieties have been shown to carry out the reduction of oxygen to peroxide.[9,15,30] Nitrogen oxides, on the other hand, may inhibit the full reduction of oxygen to water by pulling protons away from the active sites.

Etching also introduces variability into the electrochemical testing results. There is a large heterogeneity between the activity of 3 samples synthesized, as evidenced by a higher standard deviation. Oxidation of the surface occurring during acid etching causes heterogeneity of chemical composition, specifically, in nitrogen concentration (Figure 1b), which may be contributing to variability in LSVs results.

The second pyrolysis has caused an increase in the half-wave potential by 30 mV, most likely due to the increased accessibility of the iron-nitrogen centers by the reactants.[9] As XPS results show, after the 2nd pyrolysis there is a large change in the distribution of nitrogen species, with nitrogen oxides being removed and nitrogen-iron active sites being exposed at the surface (Figure 1d). The chemical composition and electrochemical testing results are more consistent for each of the samples after the 2nd pyrolysis as well. The 2nd pyrolysis can be viewed as a cleaning step of removing unwanted edge sites that are inhibiting full 4e- reduction of oxygen to water.

Also, this step increases the population of pyridinic nitrogen, which is a moiety known to reduce the peroxide intermediate into water.[9]

Each successive synthesis step contributes positively towards increasing the potential at the kinetic current of 100 μA cm^{-2}, from 0.76V vs. RHE after the first pyrolysis to becoming 0.82V vs. RHE after the last processing step. The high selectivity of catalysts throughout the synthesis is confirmed by low peroxide yields, i.e., below 3.5% for the sample after the 1st pyrolysis and below 1.5% for the final PGM-free catalyst (Figure 4d).

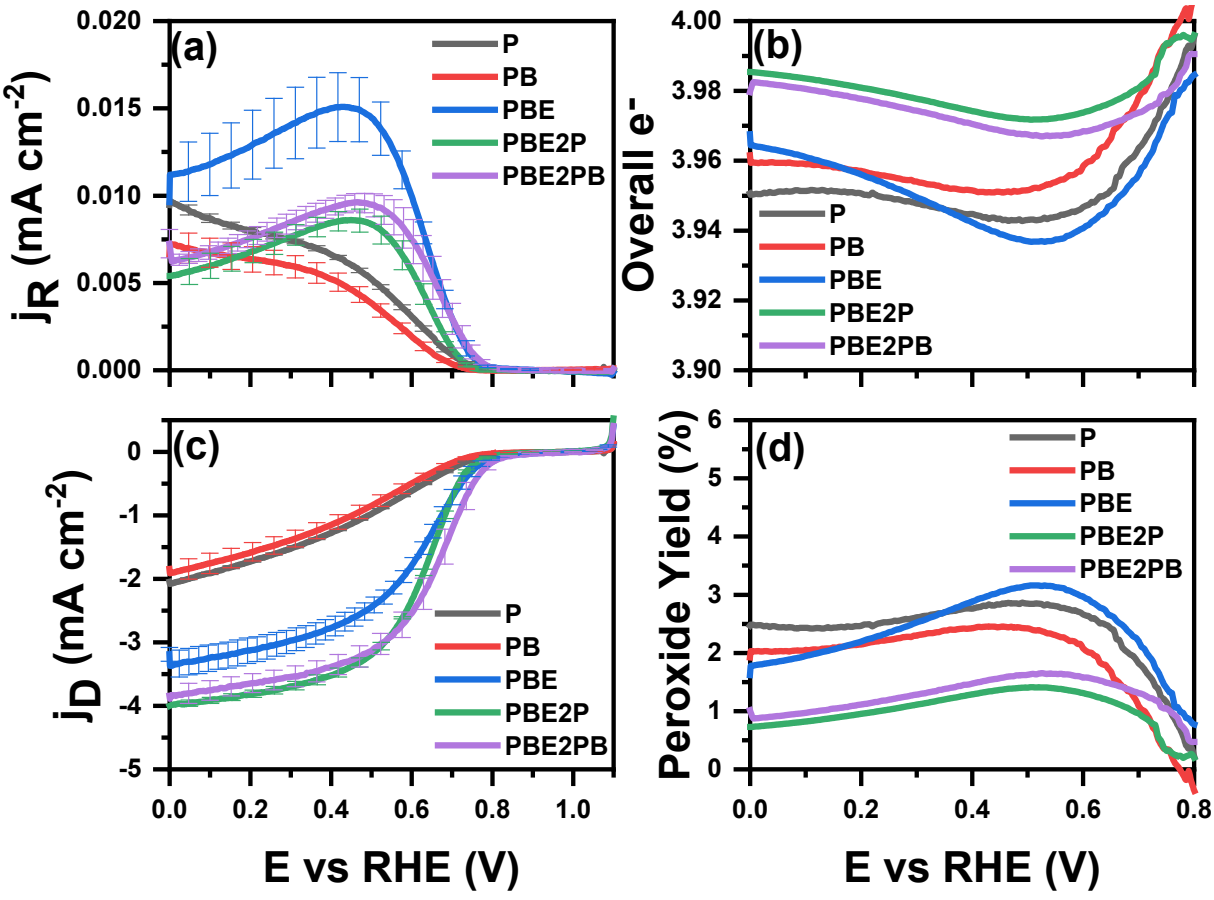

Figure 4. RRDE results in 0.5 mol L^{-1} H_2SO_4. (a) Ring current density, (b) number of electrons transferred, (c) disk current density and (d) peroxide yield %

3.3.2 ALKALINE MEDIA

The ORR activity for the PGM-free catalyst in alkaline media is presented in Figure 5, where j_R is in panel (a); overall e^- transferred in panel (b); j_D in panel (c) and peroxide yield in panel (d). Figure 5c indicates that each successive synthesis step contributes towards the increase of the potential at the kinetic current of 100μA cm^{-2} and half-wave potential of the ORR as well as the limiting current. Similarly, to the observed results in the acid media, the increase in variability between the three samples is evidenced after the acid etching, particularly for ring current (Figure 5a).

For the final synthesized PGM-free catalyst, the LSVs have potential at the kinetic current of 100μA cm^{-2} of 0.93V vs. RHE, while reaching the limiting current region at 0.6V. The onset of peroxide production is at 0.7V, the potential at which the catalyst has almost reached its limited current region. The peroxide producing species are only active at higher overpotentials. It is important to contrast this with the results for acidic media, where the onset potentials in the disk and ring are close to each other, and the peroxide yield is much lower.

The shape of the LSV of the ring current density (Figure 5a) is remarkably different for the sample after the second pyrolysis and ball milling. This is due to the transformation of the peroxide producing species during the second pyrolysis. The XPS shows a decrease in nitrogen oxides and an increase in pyridinic nitrogen, which have been found to contribute to the reduction of peroxide to water.[9] After the 2nd ball milling, some exposure of the peroxide-forming sites is occurring. This suggests the adjustment in the sequence of synthetic steps with ball milling following the acid etching and the 2nd pyrolysis being the last step of the synthesis. If some of the hydrogen-peroxide species were being formed during the ball-milling due to the energy introduced during the process,

it would be "cleaned" during the 2nd pyrolysis which showed to form pyridinic nitrogen, which also contributes to better selectivity by reducing the peroxide to water.

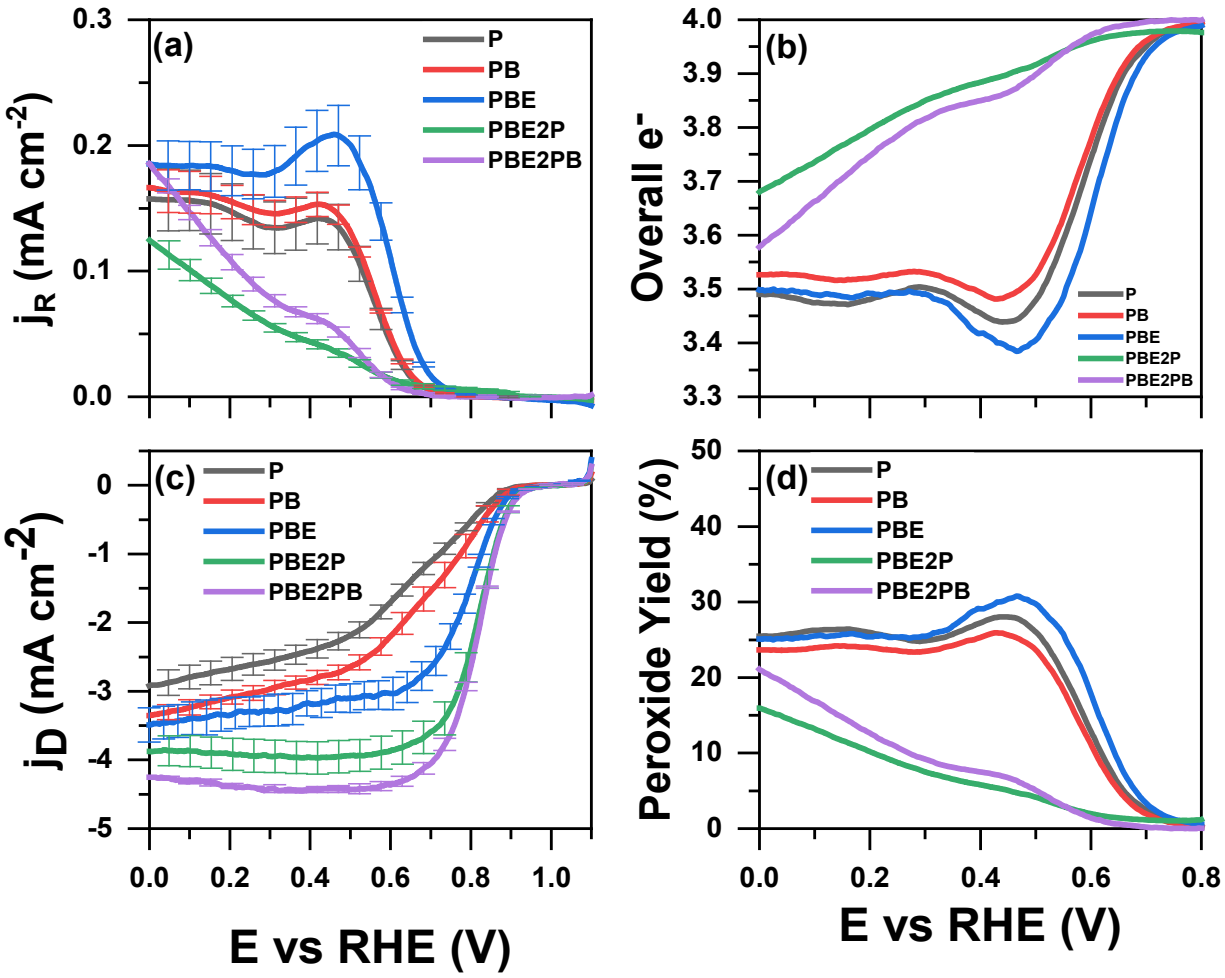

Figure 5. RRDE results in 0.1 mol L^{-1} KOH (a) Ring current density, (b) number of electrons transferred, (c) disk current density and (d) peroxide yield %

Figure 5c and 5d confirm the importance of the second pyrolysis as the step towards reducing the peroxide formation and increasing the overall number of electrons transferred. The PGM-free catalyst synthesized rapidly reaches limiting current at 0.6 V vs. RHE and has an overall electron transfer of 3.9 or a 1.5% peroxide yield at this potential (Figure 5b and 5d).

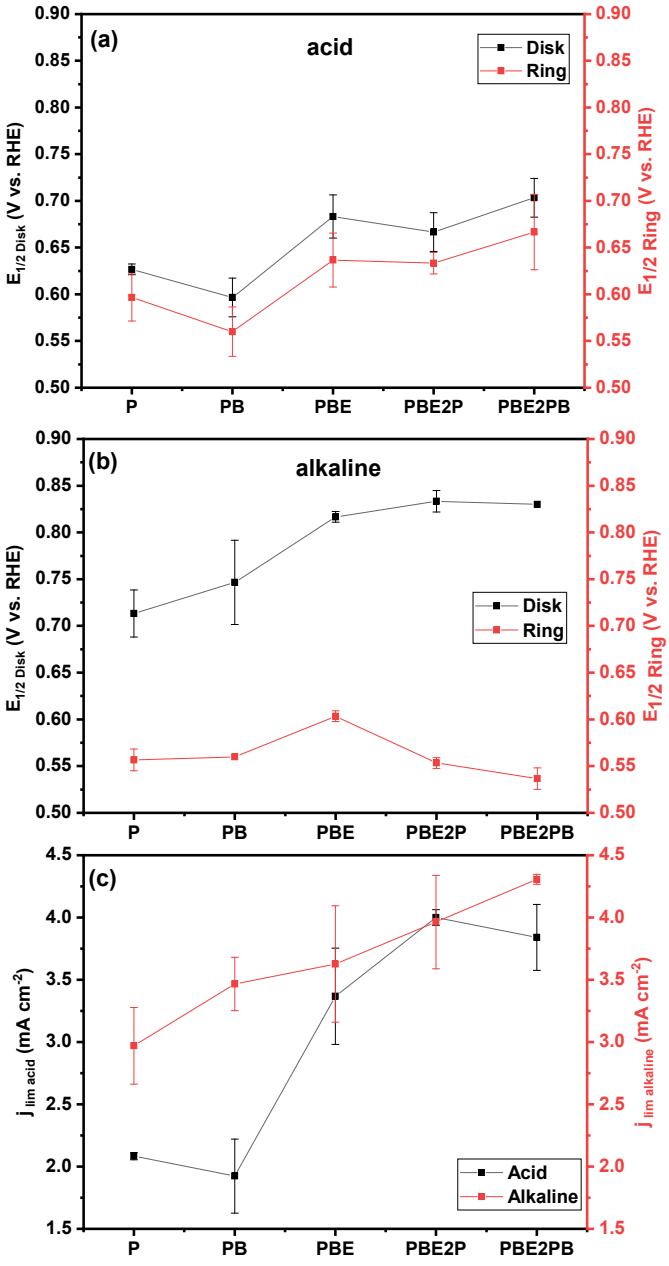

Figure 6. Half-wave potentials for the ORR in the (a) acid and (b) alkaline electrolytes. Disk limiting current density (c)

Figure 6 summarizes and compared the electrochemical performance in acidic and alkaline electrolytes evolving during each synthetic step. The half wave potentials were calculated the first derivative method from the LSVs.

The half wave potential for the disk and ring in the acid electrolyte (Figure 6a) follow a similar trend, indicating that the chemical moieties responsible for the peroxide formation are active at the same overpotentials as the ones responsible for the 4 electron transfer process. This shows that the ORR is occurring via a $4e^-$ a process with the peroxide being produced coming from the incomplete ORR carried out by some of the nitrogen species. The highest increase in the half-wave potential for the acid electrolyte happens after the etching of the

sacrificial support, indicating that the accessibility of active sites within the porous framework of the PGM-free catalyst plays an important role in the catalytic activity.

The ring half-wave potential in alkaline media (Figure 6b) is much lower than the one of the disk. Each synthesis steps increases the half wave potential, enhancing the ORR catalytic activity. The second pyrolysis reduces the half-wave potential for the ring, indicating the conversion of peroxide forming species into peroxide reducing moieties, most likely being from NO_x to pyridinic nitrogen atoms as it is evidenced by XPS analysis. Figure 2S shows that the pyridinic nitrogen moieties increased after the second pyrolysis, while the NO_x moieties decreased.

The disk half-wave potentials in the alkaline electrolyte are higher than the ones for the acid media for all the steps on the synthesis, which is quite expected.

Limiting current density for disk electrode (Figure 6c) shows different behavior for acid and alkaline. In acid, a dramatic increase in j_{lim} is observed after the acid leaching step, while for the alkaline very gradual increase with each step of the synthesis is seen. Diverse mechanisms of oxygen reduction in acid and alkaline electrolyte may be responsible for this difference.[10] In alkaline media, outer sphere mechanism is dominant,[53] so the surface of the catalyst after the 1st pyrolysis already has enough of the active sites such as surface oxides to catalyze the reaction.[10] In acidic media, the inner sphere reaction mechanism is predominant, so the chemistry of the active site is much more important. Only after the etching of silica support, the reactants can access the unique active sites that specifically selective towards ORR.

It is worth highlighting the importance of the correct catalyst loading selection for the analysis of the results obtained. Other authors[54] and ourselves[55] have performed loading studies on PGM-free catalysts. Within the first reference,[54] it is shown that the ring current density progressively increases from the lower loadings until it an intermediate loading of about 160 μg cm^{-2}, were the

ring current density reaches a maximum, expected due to the increased number of active sites with increased loading. This is an indicator that the peroxide being formed by the disk is being detected by the ring. As the catalyst loading goes from 160 μg cm^{-2} to 400 μg cm^{-2} and after that, it can be seen a significant decrease in the ring current density, which suggests that the hydrogen peroxide formed on the disk is either being further reduced to water or being disproportionated to oxygen due to the thick catalyst layer effect. The discussed loading of 160 μg cm^{-2} is very close to our optimized loading of 175 μg cm^{-2}.

The loading study[55] performed in our laboratory on a previous generation catalyst showed that the ring current density does not decrease until the loading is higher than 200 μg cm^{-2}, reinforcing the idea that the loading of 175 μg cm^{-2} elected for experiment reported herein allows for the correct assessment of the peroxide formed on the disk. The maximum in the ring current density observed at loadings of 200 μg cm^{-2} indicate that to report the current densities in relationship to geometric area, it is necessary to ensure complete coverage of the disk, and this is only happening when the loadings are approaching 200 μg cm^{-2}, as was previously established.[10]

3.4 PRINCIPAL COMPONENT ANALYSIS

The evolution of chemistry and performance during each of the synthesis steps is captured in the PCA biplot which shows a correlation between surface chemical composition and electrochemical performance in acidic and alkaline electrolytes (Figure 7). Biplots, as shown in Figure 7, allow for visualization of the clustering of samples and for identification of variables that are most/least important for these groups of samples. The variables (properties such as chemical composition, morphological metrics and electrochemical performance) that have larger magnitude for a specific group of samples are positioned closely to that group on a biplot.

Principal component #1 captures most of the variance in the data (~61%) and describes the difference between samples after Pyrolysis 1 and after the first Ball Milling (located on the negative axis of PC1) from the other samples which are located on the positive axis of PC1.

Based on variables located in each cluster of the samples on the biplot, we can see that the catalysts after the first pyrolysis and ball milling have a large amount of oxygen and surface oxides, iron with a residual amount of Fe oxides and a large amount of protonated nitrogen and amines. As was discussed above, etching results in creating an abundance of nitrous oxides at the surface, expected due to the strong oxidant nature of the nitric acid used in this step. There is a correlation in half-wave potential and limiting current densities in both acid and alkaline media - they contribute positively into PC1 and are located near to samples after 2nd pyrolysis and ball milling. Improved performance in both media is the result of the second pyrolysis and ball milling after etching away surface oxides and residual iron oxides, with optimal chemistry consisting of the larger amount of aliphatic and graphitic carbon, nitrogen, particularly, in the iron coordinated environment and pyridinic nitrogen.

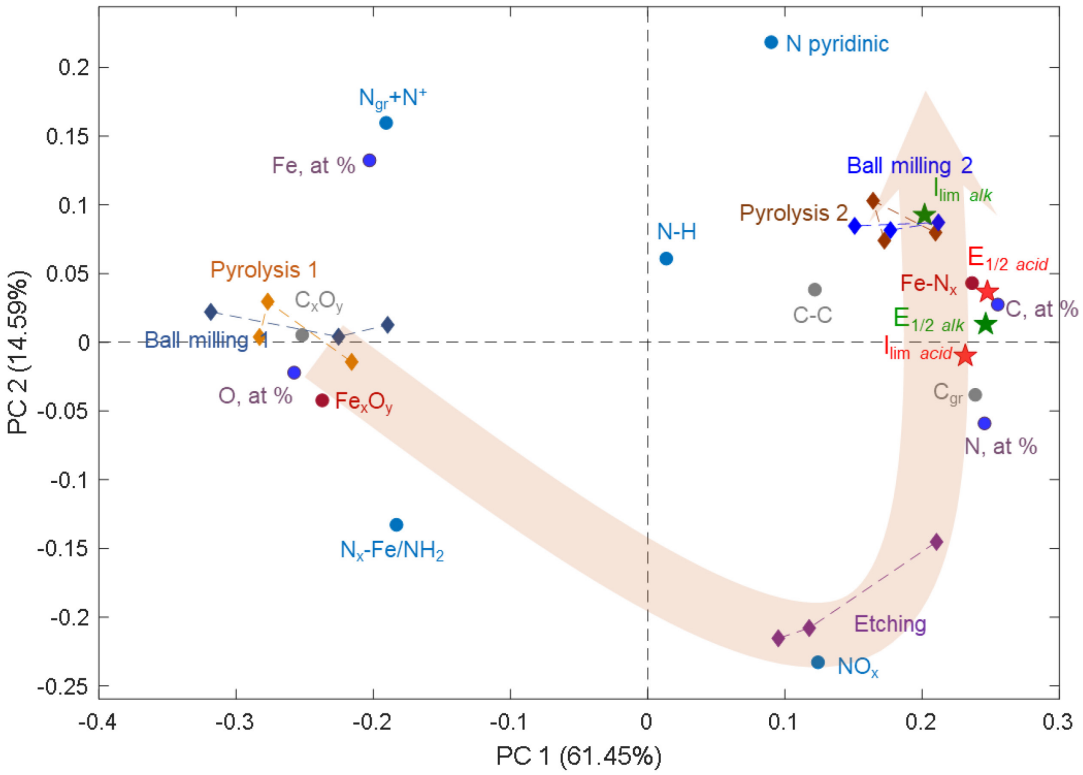

Figure 7. Correlation biplot of the evolution in PGM-free catalyst surface chemistry and electrochemical performance.

The evolution of morphology and performance during synthesis is captured by PCA biplot showing correlations between morphology and performance in Figure 8. Principal component #1 captures ~55% of the variance in the data and separates the samples after Pyrolysis 1 and Ball Milling 1 (contribute negatively to PC1) and the other samples (contribute positively into PC1). The 2nd principal component captures 30% of the variance in the data and separates samples with small solid size and pore size (contributing positively into PC2) from the samples with the smallest pore and solid size (sample after etching which contribute negatively into PC2). Initial morphology obtained after the first pyrolysis and ball milling results in the morphology lacking the properties necessary for good performance in both acidic and alkaline media, as the sacrificial support has

not been etched away, hindering the direct exposure of the active sites. Large overall area porosity formed contributes to larger hydrogen peroxide production in alkaline. The morphology that is beneficial for high half-wave potentials and high limiting current densities in both media is represented by the smaller amount of mesopores and balance between the solid size and pore dimensions.

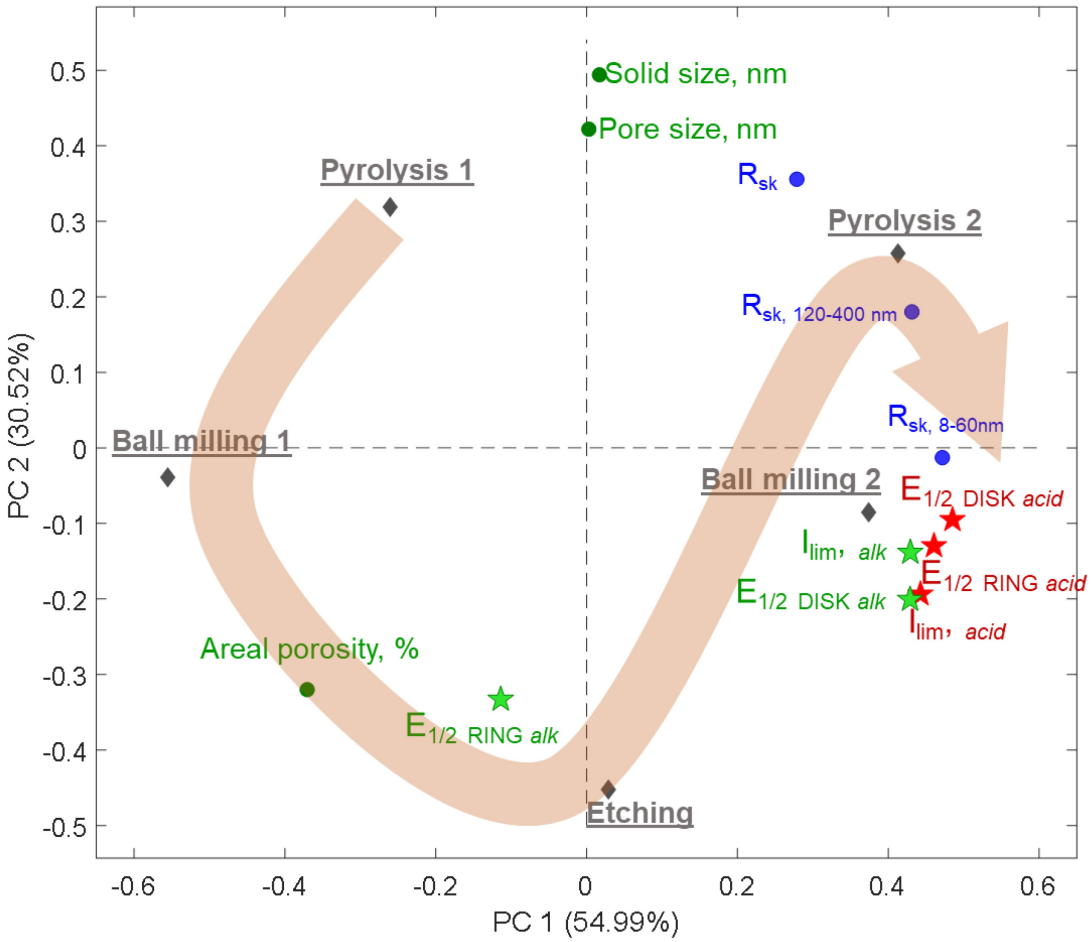

Figure 8. Correlation biplot of the evolution in PGM-free catalyst morphology and electrochemical performance.

3.5 CORRELATIONS IN ACIDIC AND ALKALINE MEDIA

Direct structure-to-property correlations were investigated by building scatter plots between metrics extracted as significant from PCA biplots and performance. As Figure 9a shows, the mesoporosity represented by skewness in the range of 8-60 nm allows for the higher number of active sites –FeN_x extracted from high-resolution Fe 2p spectra and graphitic carbon. Figure 9b confirms that the iron coordinated to nitrogen embedded within the graphitic carbon matrix is the active site that is predominantly located on the mesopores ranging between 8-60 nm, contributing to better performance in both acidic and alkaline media.

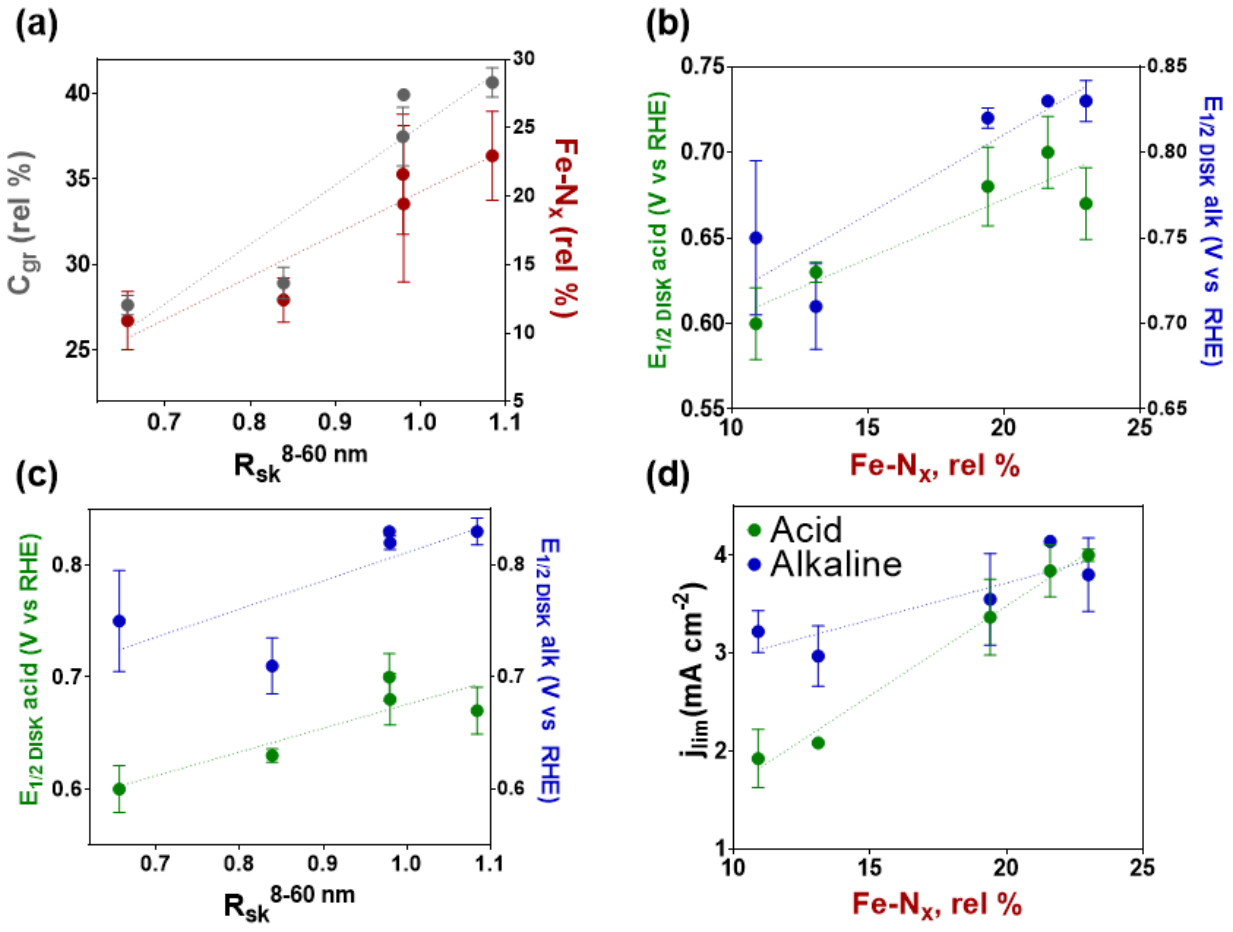

Figure 9. Important correlations of surface chemistry, morphology and electrochemical activity of the PGM-free catalyst in acid and an alkaline electrolyte. a) Surface concentration of graphitic

carbon and iron coordinated to nitrogen versus meso-skewness; half-wave potential in acid and alkaline vs b) surface concentration of Fe-Nx species and c) meso-skewness; d) limiting current density in acid and alkaline versus surface concentration of Fe-Nx species.

There is a weak direct dependence of performance in both acid and alkaline on mesoporosity shown in Figure 9c. The difference in the mechanism of oxygen reduction in acid and alkaline media is well captured in Figure 9d which shows a much larger effect of the density of sites on activity in acid than in alkaline.

4. CONCLUSIONS

This work studies the physical and chemical processing steps that the PGM-free catalysts undergo during their synthesis and the contribution towards an increased ORR catalytic activity. The surface chemistry and morphology are correlated with the electrochemical activity. Image processing techniques were applied to determine the morphological changes that the catalyst undergo through the synthesis steps. The large heterogeneity in the porosity at each synthesis step indicates that this is a parameter that needs to be further studied to get better control of the morphology of the obtained PGM-free catalyst, as this is an important factor that contributes to the active site utilization and the mass transport of the reagents and products. It was found that the acid etching and second pyrolysis are the synthesis steps which cause more uniform morphology with balance of mero- and macro-pores.

In acid electrolyte, the etching of the silica template is the major contributor to the enhancement of the half wave potential, as the ORR active sites formed during the first pyrolysis are made accessible. Further processing steps serve to increase the 4e- transfer sites, hence increasing the half-wave potential.

In alkaline electrolyte, the second pyrolysis is a critical step that favors the increased reduction of oxygen to water, as the peroxide production is significantly diminished after this step. The decrease in peroxide yield after the second pyrolysis corresponds to an increase in pyridinic nitrogen, which highlights the importance of this chemical moiety for the further reduction of peroxide into water.

The understanding of the effects of each of the synthesis steps towards the chemical composition, morphology and ORR activity of the PGM-free catalyst helps to design new synthesis processes that can increase the catalysts' performance.

ASSOCIATED CONTENT

The associated content has (I) the High resolution N 1s, C 1s and Fe 2p spectra that have been curve fitted to extract chemical speciation information, (II) the average elemental composition and chemical speciation for N 1s and C 1s along with standard deviation, (III) the overall elemental composition at all steps, (IV) Plot of relative concentration of pyridinic N versus NOx, (V) The ring and disk current density of the PGM-free catalysts for the triplicates that were tested through the five synthesis steps in acid and alkaline media and (VI) histograms of SEM images for original and filtered components.

CORRESPONDING AUTHOR

*kartyush@unm.edu.

AUTHOR CONTRIBUTIONS

The manuscript was written through the contributions of all authors. All authors have given approval to the final version of the manuscript.

[1]These authors contributed equally.

ACKNOWLEDGMENT

This work was supported by Center for MicroEngineered Materials and NSF award # 1738386 RII Track-4: Operando Analysis of Fuel Cell Materials at Advanced Light Source.

REFERENCES

(1) Kabir, S.; Serov, A.; Atanassov, P. *3D-Graphene Supports for Palladium Nanoparticles: Effect of Micro/Macropores on Oxygen Electroreduction in Anion Exchange Membrane Fuel Cells*. *J. Power Sources* **2018**, *375*, 255–264.

(2) Singh, S. K.; Takeyasu, K.; Nakamura, J. *Active Sites and Mechanism of Oxygen Reduction Reaction Electrocatalysis on Nitrogen-Doped Carbon Materials*. *Adv. Mater.* **2018**, *0*, 1804297.

(3) Jaouen, F.; Jones, D.; Coutard, N.; Artero, V.; Strasser, P.; Kucernak, A. *Toward Platinum Group Metal-Free Catalysts for Hydrogen/Air Proton-Exchange Membrane Fuel Cells*. *Johnson Matthey Technol. Rev.* **2018**, *62*, 231–255.

(4) Wu, G. *Current Challenge and Perspective of PGM-Free Cathode Catalysts for PEM Fuel Cells*. *Front. Energy* **2017**, *11*, 286–298.

(5) Serov, A. A.; Kwak, C. *Synthesis, Characterization and Catalytic Activity of RuFeSe/C as*

a Cathode Catalyst for Low-Temperature Fuel Cells. *Catal. Commun.* **2009**, *10*, 1551–1554.

(6) Serov, A. A.; Min, M.; Chai, G.; Han, S.; Kang, S.; Kwak, C. *Preparation, Characterization, and High Performance of RuSe/C for Direct Methanol Fuel Cells*. *J. Power Sources* **2008**, *175*, 175–182.

(7) Serov, A. A.; Cho, S. Y.; Han, S.; Min, M.; Chai, G.; Nam, K. H.; Kwak, C. *Modification of Palladium-Based Catalysts by Chalcogenes for Direct Methanol Fuel Cells*. *Electrochem. commun.* **2007**, *9*, 2041–2044.

(8) Kneebone, J. L.; Daifuku, S. L.; Kehl, J. A.; Wu, G.; Chung, H. T.; Hu, M. Y.; Alp, E. E.; More, K. L.; Zelenay, P.; Holby, E. F.; Neidig, M. L. *A Combined Probe-Molecule, Mössbauer, Nuclear Resonance Vibrational Spectroscopy, and Density Functional Theory Approach for Evaluation of Potential Iron Active Sites in an Oxygen Reduction Reaction Catalyst*. *J. Phys. Chem. C* **2017**, *121*, 16283–16290.

(9) Artyushkova, K.; Serov, A.; Rojas-Carbonell, S.; Atanassov, P. *Chemistry of Multitudinous Active Sites for Oxygen Reduction Reaction in Transition Metal-Nitrogen-Carbon Electrocatalysts*. *J. Phys. Chem. C* **2015**, *119*, 25917–25928.

(10) Rojas-Carbonell, S.; Artyushkova, K.; Serov, A.; Santoro, C.; Matanovic, I.; Atanassov, P. *Effect of PH on the Activity of Platinum Group Metal-Free Catalysts in Oxygen Reduction Reaction*. *ACS Catal.* **2018**, *8*, 3041–3053.

(11) Artyushkova, K.; Workman, M. J.; Matanovic, I.; Dzara, M. J.; Ngo, C.; Pylypenko, S.; Serov, A.; Atanassov, P. *Role of Surface Chemistry on Catalyst/Ionomer Interactions for*

Transition Metal–Nitrogen–Carbon Electrocatalysts. *ACS Appl. Energy Mater.* **2017**, *1*, 68–77.

(12) Capuano, C. B.; Yamaguchi, S.; Mukerjee, S.; Kishi, H.; Artyushkova, K.; Atanassov, P.; Serov, A.; Sakamoto, T.; Danilovic, N.; Doan, H. *Application of X-Ray Photoelectron Spectroscopy to Studies of Electrodes in Fuel Cells and Electrolyzers*. *J. Electron Spectros. Relat. Phenomena* **2017**, *231*, 127–139.

(13) Artyushkova, K.; Matanovic, I.; Halevi, B.; Atanassov, P. *Oxygen Binding to Active Sites of Fe-N-C ORR Electrocatalysts Observed by Ambient-Pressure XPS*. *J. Phys. Chem. C* **2017**, *121*, 2836–2843.

(14) Artyushkova, K.; Pylypenko, S.; Olson, T. S.; Fulghum, J. E.; Atanassov, P. *Predictive Modeling of Electrocatalyst Structure Based on Structure-to-Property Correlations of X-Ray Photoelectron Spectroscopic and Electrochemical Measurements*. *Langmuir* **2008**, *24*, 9082–9088.

(15) Chen, Y.; Artyushkova, K.; Rojas-Carbonell, S.; Serov, A.; Matanovic, I.; Santoro, C.; Asset, T.; Atanassov, P. *Inhibition of Surface Chemical Moieties by Tris(Hydroxymethyl)Aminomethane: A Key to Understanding Oxygen Reduction on Iron–Nitrogen–Carbon Catalysts*. *ACS Appl. Energy Mater.* **2018**, *1*, 1942–1949.

(16) Tylus, U.; Jia, Q.; Strickland, K.; Ramaswamy, N.; Serov, A.; Atanassov, P.; Mukerjee, S. *Elucidating Oxygen Reduction Active Sites in Pyrolyzed Metal-Nitrogen Coordinated Non-Precious-Metal Electrocatalyst Systems. J. Phys. Chem. C. Nanomater. Interfaces* **2014**, *118*, 8999–9008.

(17) Choi, C. H.; Choi, W. S.; Kasian, O.; Mechler, A. K.; Sougrati, M. T.; Brüller, S.; Strickland, K.; Jia, Q.; Mukerjee, S.; Mayrhofer, K. J. J.; Jaouen, F. *Unraveling the Nature of Sites Active toward Hydrogen Peroxide Reduction in Fe-N-C Catalysts*. *Angew. Chem. Int. Ed.* **2017**, *56*, 8809–8812.

(18) Matanovic, I.; Artyushkova, K.; Atanassov, P. *Understanding PGM-Free Catalysts by Linking Density Functional Theory Calculations and Structural Analysis: Perspectives and Challenges*. *Curr. Opin. Electrochem.* **2018**, *9*, 137–144.

(19) Holby, E. F.; Zelenay, P. *Linking Structure to Function: The Search for Active Sites in Non-Platinum Group Metal Oxygen Reduction Reaction Catalysts*. *Nano Energy* **2016**, *29*, 54–64.

(20) Artyushkova, K.; Kiefer, B.; Halevi, B.; Knop-Gericke, A.; Schlogl, R.; Atanassov, P. *Density Functional Theory Calculations of XPS Binding Energy Shift for Nitrogen-Containing Graphene-like Structures*. *Chem. Commun.* **2013**, *49*, 2539–2541.

(21) Chung, H. T.; Cullen, D. A.; Higgins, D.; Sneed, B. T.; Holby, E. F.; More, K. L.; Zelenay, P. *Direct Atomic-Level Insight into the Active Sites of a High-Performance PGM-Free ORR Catalyst*. *Science (80-.).* **2017**, *357*, 479–484.

(22) Matanovic, I.; Artyushkova, K.; Strand, M. B.; Dzara, M. J.; Pylypenko, S.; Atanassov, P. *Core Level Shifts of Hydrogenated Pyridinic and Pyrrolic Nitrogen in the Nitrogen-Containing Graphene-Based Electrocatalysts: In-Plane vs Edge Defects*. *J. Phys. Chem. C* **2016**, *120*, 29225–29232.

(23) Kabir, S.; Artyushkova, K.; Serov, A.; Kiefer, B.; Atanassov, P. *Binding Energy Shifts for*

Nitrogen-Containing Graphene-Based Electrocatalysts - Experiments and DFT Calculations. *Surf. Interface Anal.* **2016**, *48*, 293–300.

(24) Kabir, S.; Artyushkova, K.; Kiefer, B.; Atanassov, P. *Computational and Experimental Evidence for New TM-N3/C Moiety Family in Non-PGM Electrocatalysts . Phys. Chem. Chem. Phys.* **2015**, *17*, 17785–17789.

(25) Matanovic, I.; Atanassov, P.; Kiefer, B.; Garzon, F. H.; Henson, N. J. *Applicability of Density Functional Theory in Reproducing Accurate Vibrational Spectra of Surface Bound Species*. *J. Comput. Chem.* **2014**, *35*, 1921–1929.

(26) Kattel, S.; Atanassov, P.; Kiefer, B. *A Density Functional Theory Study of Oxygen Reduction Reaction on Non-PGM Fe–Nx–C Electrocatalysts*. *Phys. Chem. Chem. Phys.* **2014**, *16*, 13800.

(27) Holby, E. F.; Wu, G.; Zelenay, P.; Taylor, C. D. *Structure of Fe-Nx-C Defects in Oxygen Reduction Reaction Catalysts from First-Principles Modeling*. *J. Phys. Chem. C* **2014**, *118*, 14388–14393.

(28) Zhu, H.; Paddison, S. J.; Zawodzinski, T. A. *The Effects of the Ligand, Central Metal, and Solvent on the O2 Binding of Non-Precious Metal Catalyst Model Systems: An Ab Initio Study*. *Electrochim. Acta* **2013**, *101*, 293–300.

(29) Wu, G.; Johnson, C. M.; Mack, N. H.; Artyushkova, K.; Nelson, M.; Ferrandon, M.; Lezama-Pacheco, J. S.; More, K. L.; Myers, D. J.; Zelenay, P. *Synthesis-Structure-Performance Correlation for Polyaniline-Me-C Non-Precious Metal Cathode Catalysts for Oxygen Reduction in Fuel Cells*. *J. Mater. Chem.* **2011**, *21*, 11392–11405.

(30) Chen, Y.; Matanovic, I.; Weiler, E.; Atanassov, P.; Artyushkova, K. *Mechanism of Oxygen Reduction Reaction on Transition Metal–Nitrogen–Carbon Catalysts: Establishing the Role of Nitrogen-Containing Active Sites*. *ACS Appl. Energy Mater.* **2018**, *1*, 5948–5953.

(31) Workman, M. J.; Dzara, M.; Ngo, C.; Pylypenko, S.; Serov, A.; McKinney, S.; Gordon, J.; Atanassov, P.; Artyushkova, K. *Platinum Group Metal-Free Electrocatalysts: Effects of Synthesis on Structure and Performance in Proton-Exchange Membrane Fuel Cell Cathodes*. *J. Power Sources* **2017**, *348*, 30–39.

(32) Singh, K.; Razmjooei, F.; Yu, J.-S. *Active Sites and Factors Influencing Them for Efficient Oxygen Reduction Reaction in Metal-N Coordinated Pyrolyzed and Non-Pyrolyzed Catalysts: A Review*. *J. Mater. Chem. A* **2017**, *5*, 20095–20119.

(33) Kramm, U. I.; Herranz, J.; Larouche, N.; Arruda, T. M.; Lefevre, M.; Jaouen, F.; Bogdanoff, P.; Fiechter, S.; Abs-Wurmbach, I.; Mukerjee, S.; Dodelet, J.-P. P. *Structure of the Catalytic Sites in Fe/N/C-Catalysts for O2-Reduction in PEM Fuel Cells*. *Phys. Chem. Chem. Phys.* **2012**, *14*, 11673–11688.

(34) Mamtani, K.; Jain, D.; Zemlyanov, D.; Celik, G.; Luthman, J.; Renkes, G.; Co, A. C.; Ozkan, U. S. *Probing the Oxygen Reduction Reaction Active Sites over Nitrogen-Doped Carbon Nanostructures (CNx) in Acidic Media Using Phosphate Anion*. *ACS Catal.* **2016**, *6*, 7249–7259.

(35) Workman, M. J.; Serov, A.; Tsui, L. K.; Atanassov, P.; Artyushkova, K. *Fe-N-C Catalyst Graphitic Layer Structure and Fuel Cell Performance*. *ACS Energy Lett.* **2017**, *2*, 1489–1493.

(36) Busch, M.; Halck, N. B.; Kramm, U. I.; Siahrostami, S.; Krtil, P.; Rossmeisl, J. *Beyond the Top of the Volcano? – A Unified Approach to Electrocatalytic Oxygen Reduction and Oxygen Evolution*. *Nano Energy* **2016**, *29*, 126–135.

(37) Martinez, U.; Komini Babu, S.; Holby, E. F.; Zelenay, P. *Durability Challenges and Perspective in the Development of PGM-Free Electrocatalysts for the Oxygen Reduction Reaction*. *Curr. Opin. Electrochem.* **2018**, *9*, 224–232.

(38) Borup, R.; Meyers, J.; Pivovar, B.; Kim, Y. S.; Mukundan, R.; Garland, N.; Myers, D.; Wilson, M.; Garzon, F.; Wood, D.; Zelenay, P.; More, K.; Stroh, K.; Zawodzinski, T.; Boncella, J.; McGrath, J. E.; Inaba, M.; Miyatake, K.; Hori, M. *Scientific Aspects of Polymer Electrolyte Fuel Cell Durability and Degradation*. *Chem. Rev.* **2007**, *107*, 3904–3951.

(39) Santoro, C.; Rojas-Carbonell, S.; Awais, R.; Gokhale, R.; Kodali, M.; Serov, A.; Artyushkova, K.; Atanassov, P. *Influence of Platinum Group Metal-Free Catalyst Synthesis on Microbial Fuel Cell Performance*. *J. Power Sources* **2018**, *375*, 11–20.

(40) Workman, M. J.; Serov, A.; Halevi, B.; Atanassov, P.; Artyushkova, K. *Application of the Discrete Wavelet Transform to SEM and AFM Micrographs for Quantitative Analysis of Complex Surfaces*. *Langmuir* **2015**, *31*, 4924–4933.

(41) Rojas-Carbonell, S.; Babanova, S.; Serov, A.; Artyushkova, K.; Workman, M. J.; Santoro, C.; Mirabal, A.; Calabrese Barton, S.; Atanassov, P. *Integration of Platinum Group Metal-Free Catalysts and Bilirubin Oxidase into a Hybrid Material for Oxygen Reduction: Interplay of Chemistry and Morphology*. *ChemSusChem* **2017**, *10*, 1534–1542.

(42) Artyushkova, K.; Pylypenko, S.; Dowlapalli, M.; Atanassov, P. *Use of Digital Image*

Processing of Microscopic Images and Multivariate Analysis for Quantitative Correlation of Morphology, Activity and Durability of Electrocatalysts. *RSC Adv.* **2012**, *2*, 4304–4310.

(43) Artyushkova, K.; Atanassov, P.; Dutta, M.; Wessel, S.; Colbow, V. *Structural Correlations: Design Levers for Performance and Durability of Catalyst Layers*. *J. Power Sources* **2015**, *284*, 631–641.

(44) Reshetenko, T. V; St-Pierre, J.; Artyushkova, K.; Rocheleau, R.; Atanassov, P.; Bender, G.; Ulsh, M. *Multianalytical Study of the PTFE Content Local Variation of the PEMFC Gas Diffusion Layer*. *J. Electrochem. Soc.* **2013**, *160*, F1305–F1315.

(45) Santoro, C.; Artyushkova, K.; Babanova, S.; Atanassov, P.; Ieropoulos, I.; Grattieri, M.; Cristiani, P.; Trasatti, S.; Li, B. K.; Schuler, A. J. *Parameters Characterization and Optimization of Activated Carbon (AC) Cathodes for Microbial Fuel Cell Application*. *Bioresour. Technol.* **2014**, *163*, 54–63.

(46) Santoro, C.; Babanova, S.; Artyushkova, K.; Cornejo, J. A.; Ista, L.; Bretschger, O.; Marsili, E.; Atanassov, P.; Schuler, A. J. *Influence of Anodes Surface Chemistry on Microbial Fuel Cells Operation*. *Bioelectrochemistry* **2015**.

(47) Herranz, J.; Jaouen, F.; Lefèvre, M.; Kramm, U. I.; Proietti, E.; Dodelet, J.-P. P.; Bogdanoff, P.; Fiechter, S.; Abs-Wurmbach, I.; Bertrand, P.; Arruda, T. M.; Mukerjee, S. *Unveiling N-Protonation and Anion-Binding Effects on Fe/N/C Catalysts for O2 Reduction in Proton-Exchange-Membrane Fuel Cells*. *J. Phys. Chem. C* **2011**, *115*, 16087–16097.

(48) Calle-Vallejo, F.; Martinez, J. I.; Rossmeisl, J. *Density Functional Studies of Functionalized Graphitic Materials with Late Transition Metals for Oxygen Reduction Reactions*. *Phys.*

Chem. Chem. Phys. **2011**, *13*, 15639–15643.

(49) Alshibli, K. A.; Alsaleh, M. I. *Characterizing Surface Roughness and Shape of Sands Using Digital Microscopy*. *J. Comput. Civ. Eng.* **2004**, *18*, 36–45.

(50) Pyun, S. I.; Rhee, C. K. *An Investigation of Fractal Characteristics of Mesoporous Carbon Electrodes with Various Pore Structures*. *Electrochim. Acta* **2004**, *49*, 4171–4180.

(51) Zitolo, A.; Goellner, V.; Armel, V.; Sougrati, M.-T.; Mineva, T.; Stievano, L.; Fonda, E.; Jaouen, F. *Identification of Catalytic Sites for Oxygen Reduction in Iron- and Nitrogen-Doped Graphene Materials*. *Nat Mater* **2015**, *14*, 937–942.

(52) Serov, A.; Artyushkova, K.; Andersen, N. I.; Stariha, S.; Atanassov, P. *Original Mechanochemical Synthesis of Non-Platinum Group Metals Oxygen Reduction Reaction Catalysts Assisted by Sacrificial Support Method*. *Electrochim. Acta* **2015**, *179*, 154–160.

(53) Ramaswamy, N.; Mukerjee, S. *Fundamental Mechanistic Understanding of Electrocatalysis of Oxygen Reduction on Pt and Non-Pt Surfaces: Acid versus Alkaline Media*. *Adv. Phys. Chem.* **2012**, *2012*, 1–17.

(54) Bonakdarpour, A.; Lefevre, M.; Yang, R.; Jaouen, F.; Dahn, T.; Dodelet, J.-P.; Dahn, J. R. *Impact of Loading in RRDE Experiments on Fe–N–C Catalysts: Two- or Four-Electron Oxygen Reduction? Electrochem. Solid-State Lett.* **2008**, *11*, B105.

(55) Robson, M. H.; Serov, A.; Artyushkova, K.; Atanassov, P. *A Mechanistic Study of 4-Aminoantipyrine and Iron Derived Non-Platinum Group Metal Catalyst on the Oxygen Reduction Reaction*. *Electrochim. Acta* **2013**, *90*, 656–665.